

Development of grain structure during friction stir welding of pure titanium

S. Mironov*, Y.S. Sato, H. Kokawa

Department of Materials Processing, Graduate School of Engineering, Tohoku University, 6-6-02 Aramaki-aza-Aoba, Sendai 980-8579, Japan

Received 26 May 2009; received in revised form 11 June 2009; accepted 14 June 2009

Available online 18 July 2009

Abstract

The microstructure evolution during friction stir welding of commercial purity titanium was studied. Material flow was found to be close to the simple-shear deformation and arose mainly from the prism slip. The grain structure evolution was shown to be a complex process including several stages. Far from the welding tool, the microstructural evolution was found to be governed by geometrical effects of strain and limited discontinuous recrystallization. In the stir zone, formation of a strong texture was shown to lead to texture-induced grain convergence, and the grain structure development was thus closely related to the texture evolution.

© 2009 Acta Materialia Inc. Published by Elsevier Ltd. All rights reserved.

Keywords: Friction stir welding; Electron backscatter diffraction; Titanium; Microstructure; Texture

1. Introduction

Friction stir welding (FSW) is an innovative joining process invented in 1991 [1]. The principle advantage of this technology is that it enables solid-state welding. As a solid-state process, FSW avoids (or limits) solidification problems associated with conventional fusion welding and thus provides defect-free welds having good service properties even in materials that are not generally considered for welding applications.

Initially, FSW was applied to aluminum alloys. Subsequently, the very successful implementation of FSW has driven the expansion of this technology to other structural materials such as magnesium and titanium alloys and steels [2]. This practical success necessitates the development of a more fundamental understanding of the FSW process, the final aim being precise control of weld properties. The first studies in the field of FSW were focused mainly on design optimization of the FSW technique. Presently, however, microstructural examination is becoming one of the key

issues in FSW. Indeed, fundamental understanding of the structural response to FSW will permit prediction (and potentially control) of the final weld structure and, therefore, the service properties of the welds.

In the past few years, several studies have been conducted with the aim of clarifying the grain structure evolution during FSW; typically, these research attempts have focused on face-centered cubic (fcc) and body-centered cubic (bcc) metals (e.g. Refs. [3–6]). It has been shown that the grain structure development is usually a complex process which may be governed by geometrical recrystallization [3], continuous recrystallization (e.g. Ref. [4]) and grain subdivision [5]. It has also been conclusively demonstrated that the material flow during FSW may be described in terms of simple-shear deformation [3–7].

It should be pointed out that comparatively little attention has been given to hexagonal close-packed (hcp) metals despite their significant industrial importance. These materials usually have a limited number of independent slip systems which cannot provide an accommodation of arbitrary plastic strain, and this may have a substantial impact on the grain structure evolution. In FSW, investigation of the microstructural development in α -titanium is particularly challenging. Due to increased requirements of the tool

* Corresponding author. Tel.: +81 22 795 7353; fax: +81 22 795 7352.
E-mail addresses: S-72@mail.ru, smironov@material.tohoku.ac.jp (S. Mironov).

material, high tool loads and high reactivity of titanium during the welding process, FSW of titanium alloys is a significantly more arduous process than that of aluminum or magnesium alloys. As a result, microstructural examinations of friction-stirred α -titanium have been quite limited (e.g. Refs. [8,9]). According to Lee et al. [9], the grain structure in the stir zone (SZ) of α -titanium weldments is dominated by twins and the twin fraction appears to increase towards the upper part of the weld. The microstructure is not recrystallized in appearance and the grains contain a high density of tangled dislocations mixed with dislocation subboundaries. On the other hand, Lienert [8] reported significant grain refinement in the stir zone and attributed this process to dynamic recrystallization.

The above-mentioned research efforts have provided important insights into the structural response of α -titanium to FSW. Obviously, however, more research is required to clarify the microstructural evolution in this material. In order to improve our basic physical understanding of FSW of α -titanium, the present study was focused on fundamental issues of grain structure development. For this purpose, the electron backscatter diffraction (EBSD) technique in conjunction with field emission gun scanning electron microscopy (FE-SEM) was employed in an attempt to provide a comprehensive overview of microstructural evolution during FSW of commercial purity titanium.

2. Experimental

The material used in the present investigation was commercial purity α -titanium (ASTM Grade 2) with a nominal chemical composition. This is a comparatively simple α -titanium alloy whose deformation behavior under “conventional” modes of strain has been well documented. The material was supplied as 3-mm-thick rolled sheets.

The as-received sheets were butt-welded together in the direction transverse to the rolling direction. The welding process was performed on an FSW machine fitted with an automated control system at a tool travel speed of 60 mm min⁻¹. The welding tool was fabricated from a Mo-based alloy and consisted of a convex shoulder having a diameter of 15 mm and a pin, tapered from 5.1 mm at the shoulder to 3 mm at the pin tip. During FSW, the plunge depth of the tool was controlled so as to be 2 mm, and thus partially penetrated welds were produced. In order to prevent overheating the material higher than the β -transus temperature (around 880 °C), and thus to provide material flow only in the hcp α -phase field, a relatively low tool rotational speed of 200 rpm was applied in this study. To minimize surface oxidation, argon shielding was employed around the tool during FSW. In this paper, the principal directions of FSW geometry are denoted as follows: welding direction (WD), rolling direction (RD) and normal direction (ND).

Following FSW, the obtained welds were cross-sectioned perpendicular to the WD for microstructural exam-

inations. For optical microscopy (OM) observations, the sample was ground with water abrasive paper, mechanically polished with a final polishing step comprising of 1- μ m diamond paste, and then etched in a solution of hydrofluoric acid, nitric acid and distilled water at a ratio of 1:2:3. A suitable surface finish for EBSD was obtained by applying mechanical polishing in a similar fashion followed by electro-polishing in a solution of 20% perchloric acid in acetic anhydride at approximately 15 °C with an applied potential of 60 V.

All microstructural observations were made on the transversal (i.e., RD–ND) plane. The OM studies were carried out using a Nikon Optiphot-100 optical microscope. High-resolution EBSD analysis was conducted using a Hitachi S-4300SE FE-SEM equipped with the TSL OIM™ EBSD system. Orientation mapping involving automatic beam scanning was performed using a triangular scanning grid. On each pattern, nine Kikuchi bands were used for indexing, thus minimizing the possibility of misindexing error. EBSD maps of ~300,000–600,000 pixels with step (pixel) sizes of 0.2–2.0 μ m and containing ~400–13,350 grains were obtained. Pattern solving efficiency was in the range of 99–100%. The average confidence index (CI) for each EBSD map ranged from 0.26 to 0.47. By comparison, experiments on fcc materials have shown that the fraction of correctly indexed patterns with CI's greater than 0.1 is 95% [10]. In order to ensure the reliability of the EBSD data, all small grains comprising three or fewer pixels were automatically removed from the maps using the grain-dilation option in the TSL software. To eliminate spurious boundaries caused by orientation noise, a lower limit boundary misorientation cut-off of 2° was used. All misorientation angles quoted are relative to the rotation axis with the minimum misorientation, and a 15° criterion was used to define low-angle boundaries (LABs) versus high-angle boundaries (HABs). All measurements of grain size and grain-boundary spacing were made on the EBSD maps by the linear intercept method.

All optical and EBSD micrographs were taken in the RD–ND plane and presented so that the RD was horizontal and the ND was vertical.

3. Results and discussion

3.1. Base material

Characteristic microstructural features of the as-received (base) material are summarized in Fig. 1. EBSD observations demonstrated that the initial microstructure comprised single-phase, equiaxed α -titanium with an average grain size of about 24 μ m, as shown in Fig. 1a. Most of the grain boundaries are high-angle in character (HAB fraction is ~70%) and only sporadic LABs are clustered within some grains. It is noteworthy that some grains contain wedge- and lens-shaped twins (an example is arrowed in Fig. 1a). Local misorientations across the twin–matrix interface are typically close to 85° $\langle 2\bar{1}\bar{1}0 \rangle$, thus indicating that these are

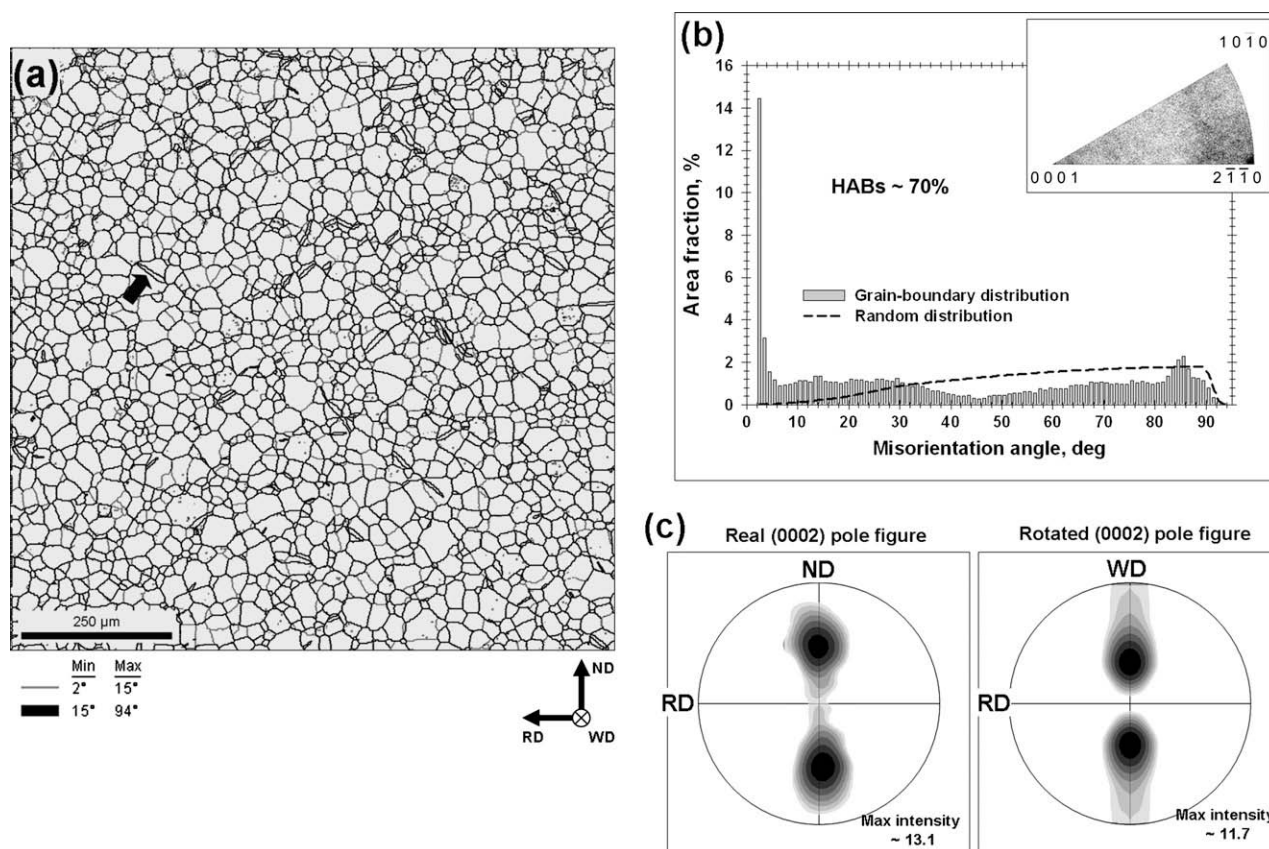


Fig. 1. Characteristic microstructural features of the base material: (a) EBSD map showing the distributions of high- and low-angle boundaries (black and gray lines, respectively); (b) misorientation distribution (misorientation-axis distribution is shown in top right corner); (c) (0 0 0 2) pole figures in RD–ND and RD–WD reference frames (WD is the transverse direction in the rolling reference frame. See text for details).

$\{10\bar{1}2\}$ twins. Misorientation distribution is characterized by a sharp low-angle peak and some clustering of the misorientation axes near the $\langle 2\bar{1}\bar{1}0 \rangle$ pole (Fig. 1b). The base material has a strong texture with a bimodal distribution of basal planes (Fig. 1c). Rotation of the measured (0 0 0 2) pole figure into a conventional reference frame for rolling (i.e., RD–WD in Fig. 1c) revealed a typical rolling texture for α -titanium with the maximal intensity at locations tilted $\sim \pm 35^\circ$ from the ND towards the WD.

3.2. Low-magnification overview

A low magnification overview of a typical transversal cross-section of a friction stir weld is shown in Fig. 2. In the figure (and throughout the paper), retreating and advancing sides of the weld are abbreviated as RS and AS, respectively.

Three distinct zones can be readily identified: the SZ, the BM and a narrow transition region – the so-called thermo-mechanically affected zone (TMAZ). The SZ exhibits a basin-like shape significantly widening towards the upper surface; this may be associated with the strong influence of the tool shoulder on material flow during FSW [11]. The SZ is not symmetric with respect to the weld line (“kissing bond” in Fig. 2), being significantly shifted

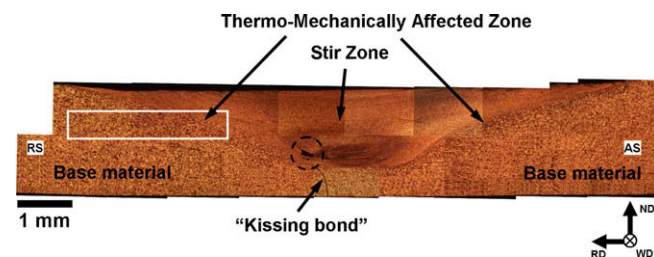


Fig. 2. Low-magnification overview of the transversal cross-section of the friction stir weld. See text for details. Note.: RS and AS are the retreating side and the advancing side, respectively.

towards the AS. This effect is well known in FSW and is usually attributed to the specific character of the tool motion during the welding process. There is an evident tunnel-type defect in the bottom part of the SZ (encircled). This defect is thought to be associated with the relatively low tool rotation speed, but detailed analysis is beyond the scope of the present study. There is no evident onion-ring structure in the SZ, but the optical contrast is not homogeneous, the bottom part of the weld being comparatively dark. The interface between the SZ and the base material is relatively diffuse on the RS of the weld, but quite sharp at the AS of the weld.

3.3. TMAZ

The transition nature of the TMAZ microstructure is a key point for understanding how the original grain structure was transformed into the SZ microstructure during FSW. In this regard, it is worth giving detailed consideration to this zone. In the present study the grain structures that developed in the TMAZ on the AS and RS were analyzed in detail. Both regions broadly showed the same general trend in microstructure evolution and, for the sake of simplicity, only the microstructure which developed on the RS is described below.

In order to provide a fundamental insight into the grain structure development, a large EBSD map was taken from the region indicated by the white rectangle in Fig. 2. The EBSD map is shown in Fig. 3a, and some selected areas are given at higher magnifications in Fig. 3b–d. In the EBSD map, individual grains are colored according to their crystallographic orientations relative to the WD; an orientation code triangle is shown in the bottom right corner. In the map, LABs are depicted as gray lines (in Fig. 3a they are omitted for the sake of simplicity), and HABs as black lines. In order to quantify the microstructural evolution towards the SZ, the large EBSD map in Fig. 3a is divided into three regions (Region 1, Region 2 and Region 3), and the microstructural data derived from these regions are summarized in Table 1 and Figs. 4 and 5.

3.3.1. Region 1

Fig. 3a demonstrates that the TMAZ extends at least 3 mm from the SZ. Near the outer edge of the TMAZ

Table 1

Average grain-boundary spacing and HAB fraction for base material and different regions shown in Fig. 3.

Microstructural region	HAB fraction (%)	HAB spacing (μm)
Base material	70	24
Region 1	29	14.7
Region 2	46	8.9
Region 3	58	8.9

(Region 1 in Fig. 3a), the original grains tend to be reoriented in the direction of tool rotation, presumably due to the geometrical requirements of strain. On the other hand, the crystallographic orientation of the parent grains does not change principally and the original two-component rolling texture can still be recognized in the (0 0 0 2) pole figure (Fig. 4a).

LABs start to develop in the grain interiors (Fig. 3b), thus drastically decreasing the total HAB fraction down to ~29% (Table 1). There is some muted tendency for the LABs to cluster near original grain boundaries, but frequently they extend across the grains (an example is arrowed). The extended LABs are reasonably straight in the grain scale and their traces are typically close to the traces of the {10 $\bar{1}$ 0} or {11 $\bar{2}$ 0} prism slip planes. A typical example of the crystallographic alignment of the LABs is illustrated in the high-magnification inset shown in the bottom right corner of Fig. 3b. It is seen that the boundary traces of the extended LABs lay close to the {10 $\bar{1}$ 0} slip plane trace which is marked by a dotted line in the figure. Another important point is the observation that the rotation axes of the LABs are typically close to the <0001>

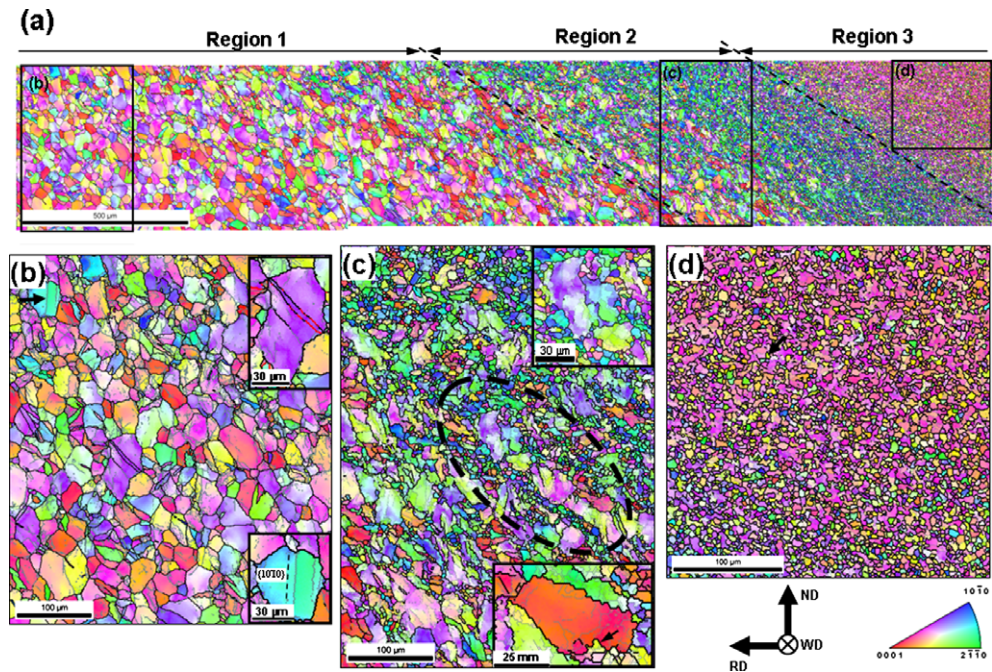


Fig. 3. Composite EBSD map of the thermo-mechanically affected zone on the retreating side of the weld (a), with selected areas shown at higher magnifications in (b–d). The individual grains are colored according to their crystallographic directions relative to WD; the color code triangle is shown in the bottom right corner. LABs and HABs are depicted as gray and black lines, respectively. See text for details.

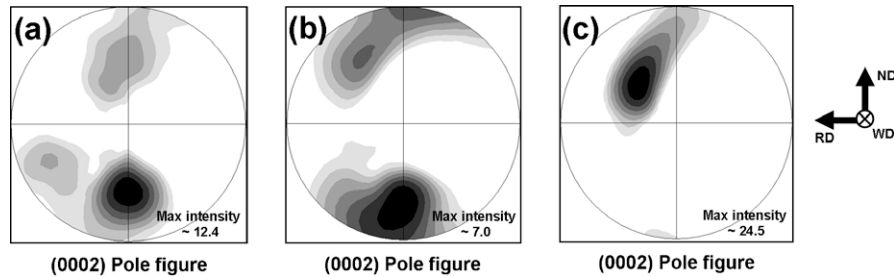


Fig. 4. The (0002) pole figures showing microtextures in Region 1 (a), Region 2 (b) and Region 3 (c).

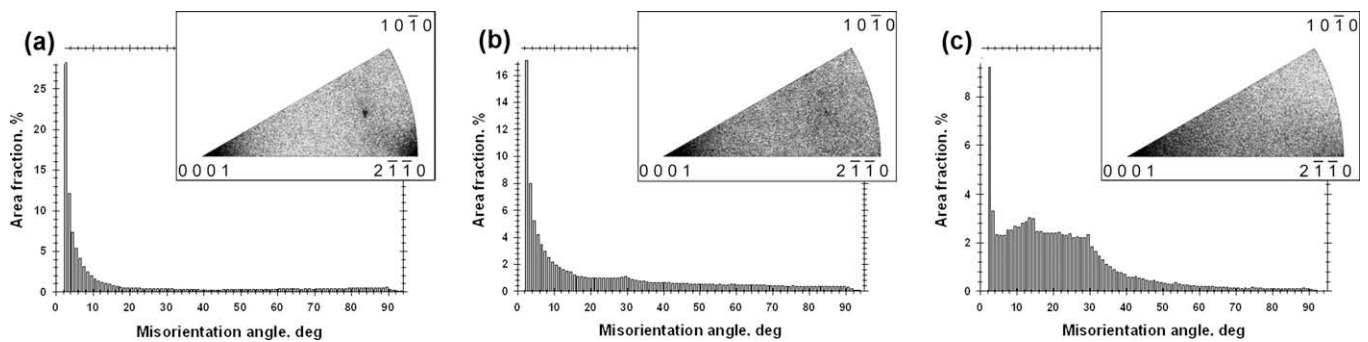


Fig. 5. Misorientation distributions in Region 1 (a), Region 2 (b) and Region 3 (c). Misorientation-axis distributions are shown in the top right corners.

pole, thus producing a strong cluster in the misorientation-axis distribution (Fig. 5a). The rotation axes of dislocation boundaries (i.e., low-angle boundaries) provide constraints on the slip systems which are potentially active during deformation. It is well accepted that slip activity of the p system rotates a crystalline lattice around the axis $w_p \parallel (b \times n)_p$, where w_p is the rotation axis, b is Burgers vector magnitude and n is the slip plane normal. Among all possible slip modes available in α -titanium (prism, basal and pyramidal), only the prism slip provides a lattice rotation around the $\langle 0001 \rangle$ axis. Thus, the proximity of the misorientation axes of the LABs to $\langle 0001 \rangle$ as well as their alignment with the prism planes indirectly indicates activity of the prism slip in Region 1. Taking into account that the prism slip is commonly accepted to be a dominant deformation mode in α -titanium, this conclusion appears to be quite reasonable.

In some cases, the extended LABs are coupled in pairs, but usually they are not arranged as well-defined boundary sets typically seen in deformed fcc and bcc metals (e.g. Refs. [12,13]). It is unlikely, therefore, that the LAB development in the present case was driven by the grain subdivision mechanism [14] in contrast to the case of fcc and bcc metals. The subboundaries within the grains are usually low-angle in nature, but some boundary segments have already accumulated misorientation exceeding 15° . Together with some compression of the original grains caused by the geometrical effects of strain, this notably decreases the average HAB spacing down to $\sim 15 \mu\text{m}$ (Table 1).

An interesting microstructural feature of Region 1 is transformation of the twin boundaries. This process is

illustrated in the high-magnification inset shown in the top right corner of Fig. 3b; in the figure, the boundaries of the $\{10\bar{1}2\}$ twins (within 5° tolerance) are highlighted by red. Misorientation across the twin boundaries starts to deviate from the exact twin/matrix relationship, and this process eventually transforms some segments of the twin boundaries into random (not twin) HABs (shown by black in the figure). This phenomenon has been already reported in the literature (e.g. Ref. [15]) and may be explained as being due to the deformation-induced crystallographic rotations of the twins and matrix from their initial orientations.

3.3.2. Region 2

In Region 2 (Fig. 3a), the original grains become thinner with higher aspect ratios, thus reflecting the strain increase towards the SZ (Fig. 3c). The boundaries of the parent grains become wavy as the temperature increases and local boundary migration starts to occur. Details of this process are illustrated in the high-magnification inset shown in the bottom right corner of Fig. 3c. It is seen that the segments of the original grain boundaries are bowed at the triple points created by transverse LABs. This phenomenon has been well described in the literature (e.g. Ref. [16]) and would be associated with the local imbalance between the low mobility of the LABs and the high mobility of the HABs. The development of local grain boundary migration gives rise to bulges along the original grain boundaries (an example is arrowed in the high-magnification inset), which eventually transform into fine grains. The high-magnification inset given in the top right corner of Fig. 3b demon-

strates that the newly developed fine grains are typically completely surrounded by HABs, have equiaxed morphology and frequently contain almost no substructure. Closer to the SZ, they notably coarsen in size and increase in volume fraction, creating a “necklace” structure decorating the elongated parent grains (an example is encircled in Fig. 3c). The microstructural behavior shown in the inset of Fig. 3c is ubiquitous throughout Region 2. The geometrical thinning of the parent grains as well as nucleation of the new fine grains significantly decrease the average HAB spacing and increase the HAB fraction in Region 2 (Table 1).

Interestingly, crystallographic orientations of the newly developed fine grains are not random, but rather typically close to $\langle 0001 \rangle \parallel \text{ND}$, which notably changes the textural pattern in Region 2 (Fig. 4b). In other words, the $\{0002\}$ basal planes in the fine grains tend to align with the tool shoulder plane. However, the reason for this phenomenon is unclear.

Thus the very specific mechanism responsible for the formation of the fine grains, involving the bulging of the original grain boundaries, nucleation of the fine equiaxed subboundaries-free grains and followed by the subsequent grain growth, indirectly indicates that the grain structure evolution in this region fits the definition of discontinuous recrystallization. In this context, the origin of the preferential near- $\langle 0001 \rangle \parallel \text{ND}$ orientation of the fine grains is not clear, thus necessitating further clarification of the microstructural mechanism governing their formation.

3.3.3. Region 3

In Region 3 (Fig. 3a), the structure morphology, texture and misorientation distribution drastically change.

The microstructure developed in this region is very specific and cannot be described adequately in conventional terms of grains (Fig. 3d). Instead, the dominant microstructural feature is an irregular mixture of HABs and LABs (Fig. 3d). The microstructure is evidently directional (Fig. 3d), tending to align roughly parallel to the border between the TMAZ and SZ. Another important microstructural component in Region 3 is fine equiaxed grains (an example is arrowed in Fig. 3d). In contrast to the HAB/LAB “matrix”, the fine grains are completely surrounded by HABs and contain almost no substructure. The texture sharpens significantly (achieving ~ 24.5 times random) and the textural pattern also becomes very specific (Fig. 4c). The misorientation distribution is also somewhat unusual and is characterized by a broad irregular maximum in the angular range of $\sim 5\text{--}50^\circ$ and clustering of the misorientation axes near $\langle 0001 \rangle$ and $\langle 2\bar{1}\bar{1}0 \rangle$ (Fig. 5c).

It should be emphasized that the transition between the Regions 2 and 3 is very sharp. Therefore, the possible microstructural mechanism responsible for the formation of the specific microstructure in Region 3 is not evident and will be discussed below.

3.4. Stir zone

3.4.1. Structure morphology

Attempting to avoid the complicated material flow that would occur near the tool shoulder and weld root, microstructural studies were focused on the SZ mid-thickness. EBSD maps showing arrangements of LABs and HABs in different locations within the SZ are summarized in Fig. 6; in the maps, the LABs are depicted as thin red lines and HABs as solid black lines.

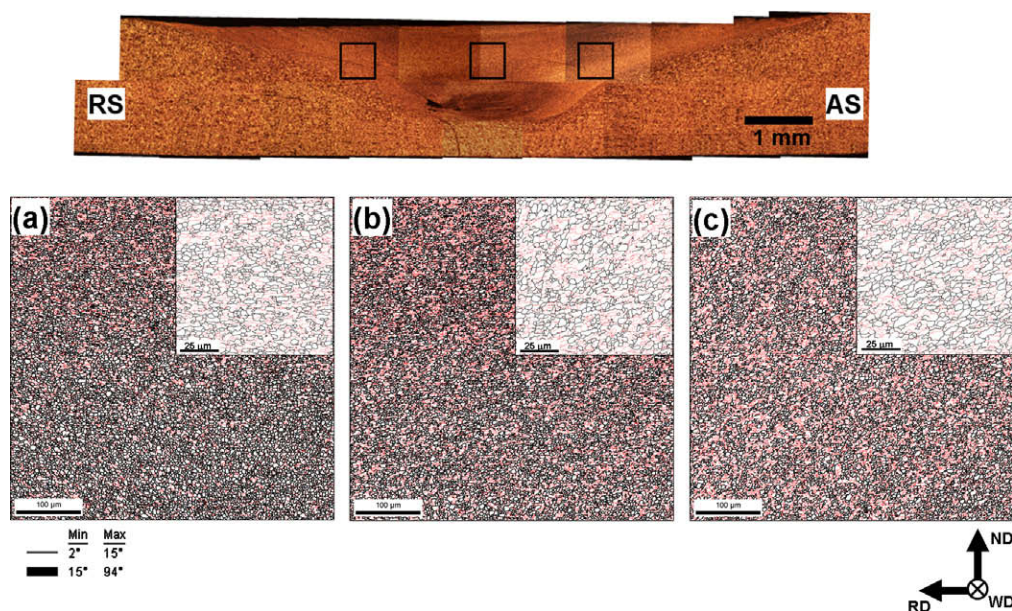


Fig. 6. EBSD maps showing arrangement of low- and high-angle boundaries in different locations within the stir zone: RS (a), center (b) and AS (c). High-resolution EBSD maps of the microstructures are given in the top right corners. In the maps, LABs are depicted as thin red lines and HABs as solid black lines. See text for details.

and HABs as solid black lines. High-resolution EBSD images acquired with a scan step size of $0.2\ \mu\text{m}$ are given in the top right corners of the maps.

The EBSD maps demonstrate that the grain structures which developed in the different locations of the SZ are broadly similar to each other as well as to those which evolved in the inner edge of the TMAZ (Fig. 3d). The low-resolution maps in Fig. 6 show that the SZ microstructures are directional, being roughly parallel to the TMAZ/SZ border. On the other hand, high-resolution maps in Fig. 6 evidence that the dominant microstructural feature of the SZ is an irregular mixture of HABs and LABs. The development of such a structural morphology has been well documented for severely deformed materials (e.g. Refs. [17,18]), which indirectly indicates that the material in the SZ has experienced significant plastic deformation. An important microstructural component of the SZ is also fine equiaxed grains. These grains typically contain almost no substructure and are completely surrounded by HABs, thus being similar to the recrystallization nuclei in Region 2 (Fig. 3c). Moving from the RS (Fig. 6a) to the central part of the SZ and AS (Fig. 6b and c), the grain structure demonstrates only geometrical realignment and a decrease in the volume fraction of the “recrystallized” grains, but the structure morphology remains relatively unchanged.

3.4.2. Texture

It is now well accepted that the microstructure evolution during large plastic deformation is closely linked to the texture evolution (e.g. Refs. [14,19]). Therefore, examination

of the texture which developed in the SZ may provide an additional insight into the grain structure evolution during FSW.

Although the material flow during FSW appears to be very complicated, the predominant deformation mode is expected to be simple shear (e.g. Refs. [3–7]). Shear textures are conventionally defined in terms of crystallographic plane and direction, aligned with the shear plane and shear direction, respectively. Ideal orientations of hcp metals (including titanium) under simple shear are given in Fig. 7a and Table 2 [20,21]; SPN is shear plane normal and SD is shear direction. However, before considering the texture developed in the SZ, it is very important to choose a proper reference frame. During FSW, the shear plane and direction are not simply related to the sample geometry, but might be expected to be approximately parallel to either the pin column surface [7], or a truncated cone having a diameter equal to the tool shoulder diameter in the top part of the SZ and the pin diameter in the bottom part of the SZ [6]. If so, the shear direction/plane should not be constant within the SZ, but would follow a curved line/surface across the SZ due to rotation of the tool. The geometrical arrangement of possible shear directions within the SZ appears to be a circle with the SD \parallel RD in the central part of the SZ, as illustrated in Fig. 7b. Orientation of the shear plane is generally not so evident, but the alignment of the SZ microstructure roughly parallel to the SZ/TMAZ border indirectly indicates that the shear plane may be nearly parallel to this border in the present study. If so, the shear surface may be expected to be close

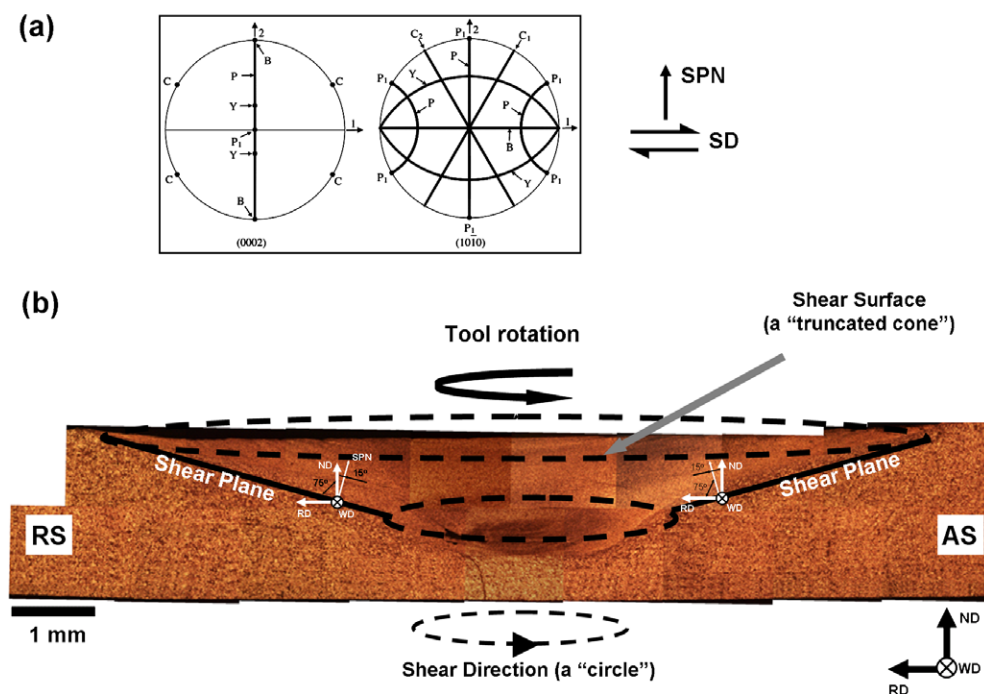


Fig. 7. (a) Ideal orientations of hcp metals under simple shear as they appear in $\{0002\}$ and $\{10\bar{1}0\}$ pole figures (after Beausir et al. [20]) and (b) schematic representation of orientations of shear plane and shear directions within the SZ. SPN and SD are shear plane normal and shear direction, respectively. See text for details.

Table 2
Main ideal orientations in simple-shear deformation of hcp metals (after Beausir et al. [20] and Li [21]).

Notation	Euler angles			$\{h k i l\} \langle u v t w \rangle$	Fiber axis and its alignment	Associated slip modes
	φ_1	ϕ	φ_2			
B-fiber	0	90	0–60	$\{0001\} \langle u v t w \rangle$	$\langle 0001 \rangle \parallel$ shear plane normal	$\{0002\} \langle 1\bar{2}10 \rangle, \{10\bar{1}1\} \langle 1\bar{2}10 \rangle, \{10\bar{1}1\} \langle \bar{1}\bar{1}23 \rangle$
P-fiber	0	0–90	0	$\{h k i l\} \langle 2\bar{1}10 \rangle$	$\langle 2\bar{1}10 \rangle \parallel$ shear direction	$\{10\bar{1}0\} \langle 1\bar{2}10 \rangle, \{0002\} \langle 1\bar{2}10 \rangle, \{10\bar{1}1\} \langle 1\bar{2}10 \rangle$
Y-fiber	0	30	30–60	$\{01\bar{1}1\} \langle 2\bar{1}10 \rangle (\varphi_2 = 0^\circ)$ $\{1\bar{1}22\} \langle 1100 \rangle (\varphi_2 = 30^\circ)$	$\langle 0001 \rangle$ is rotated towards the shear plane by $\pm 30^\circ$	$\{10\bar{1}1\} \langle 1\bar{2}10 \rangle$
C-fiber	60	90	0–60	$\{2\bar{1}12\} \langle 2\bar{1}13 \rangle (\varphi_2 = 0^\circ)$ $\{1\bar{1}01\} \langle 1\bar{1}02 \rangle (\varphi_2 = 30^\circ)$	$\langle 0001 \rangle$ is first rotated 90° , then $\pm 30^\circ$ in the shear plane direction	$\{10\bar{1}1\} \langle \bar{1}\bar{1}23 \rangle, \{11\bar{2}2\} \langle \bar{1}\bar{1}23 \rangle$

to the truncated cone, as shown in Fig. 7b. This idea is in agreement with recent investigations of the textures developed during FSW of β -titanium [6] and pure iron [5].

Orientation data derived from the low-resolution EBSD maps in Fig. 6 are arranged as $\{0002\}$ and $\{10\bar{1}0\}$ pole figures in Fig. 8a. The pole figures have the same reference directions as the maps, i.e., the ND is vertical and RD is horizontal. It should be noted that the pole figure for the RS of the SZ is broadly similar to that for Region 3 (Fig. 4c). Attempting to vertically align the assumed SPN, all the pole figures in Fig. 8a were tilted by 15° (see scheme in Fig. 7b). The rotated pole figures are summarized in Fig. 8b. It should be pointed out that the horizontal axes in the rotated pole figures are still RD. In other words, only the rotated pole figure for the central part of the SZ represents the orientation data in the conventional reference frame for the simple shear (SD is horizontal and SPN is vertical); in the rotated pole figures for RS and AS, the horizontal axis deviates from the SD.

To a first approximation, the textural pattern in the rotated pole figures taken from the central part of the SZ may be described in terms of partial P-fiber ideal simple shear texture (with a pronounced $P_1\{10\bar{1}0\}\langle 11\bar{2}0 \rangle$ component), according to the adopted convention (Fig. 7a).

The P_1 component rotates from RS to AS following the rotation of the shear direction across the SZ (see scheme in Fig. 7b). Development of the P_1 simple shear texture during FSW of near- α titanium has also been reported recently by Knippling and Fonda [22].

Formation of the P-fiber texture is associated with predominance of the prism $\{10\bar{1}0\}\langle 1\bar{2}10 \rangle$ slip with some contribution of the basal $\{0002\}\langle 1\bar{2}10 \rangle$ and $\{10\bar{1}1\}\langle 1\bar{2}10 \rangle$ pyramidal slips (Table 2). Therefore, the obtained results evidence that the material flow during FSW of α -titanium indeed arises from the simple-shear deformation (the shear surface being close to the truncated cone) and is mainly governed by the prism slip. Taking into account that the prism slip is commonly accepted to be a dominant deformation mode in α -titanium, the obtained result appears to be reasonable.

3.4.3. Misorientation distribution

Attempting to obtain a deeper insight into the microstructure developed at the various locations within the SZ, misorientation data were extracted from the low-resolution EBSD maps in Fig. 6 and arranged as grain-boundary (GB) misorientation-angle and misorientation-axis distributions in Fig. 9. In order to assess the effect of the

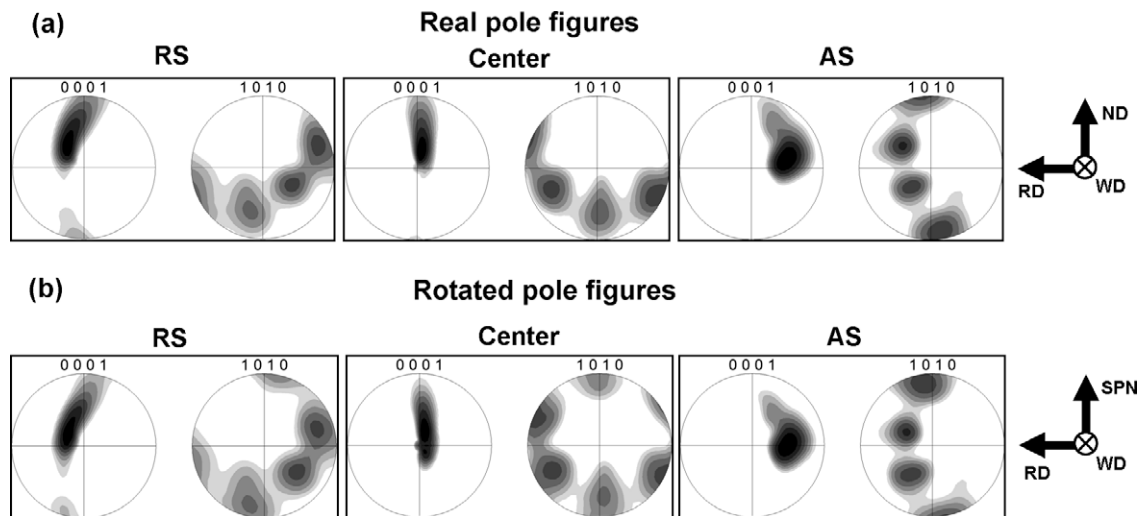


Fig. 8. Orientation data derived from the EBSD maps in Fig. 6 and arranged as $\{0002\}$ and $\{10\bar{1}0\}$ pole figures. In (a) the pole figures have the same orientations as the map (i.e., ND vertical and RD horizontal). In (b) the pole figures have been tilted by $+15^\circ$ around the RD to vertically align the assumed shear plane normal (SPN). See text for details.

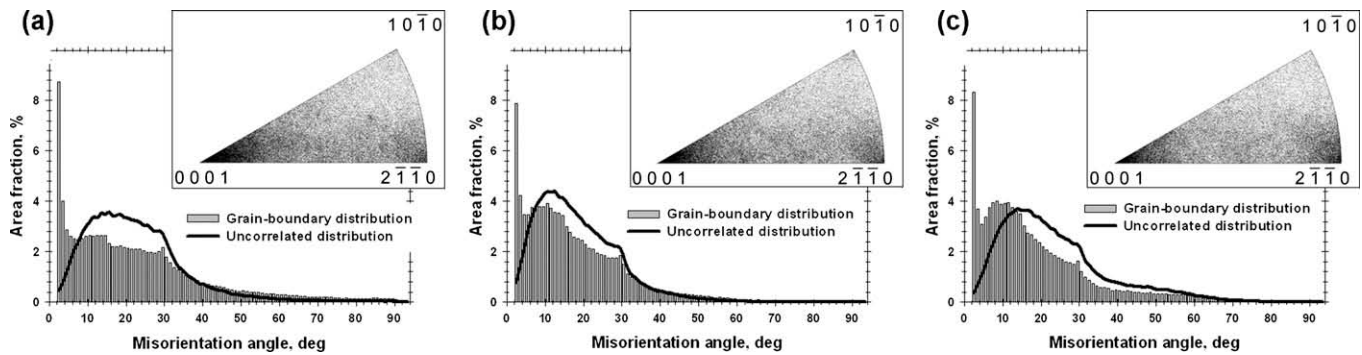


Fig. 9. Misorientation data derived from the EBSD maps in Fig. 6 and arranged as misorientation-angle and misorientation-axis distributions for RS (a), center (b) and AS (c). Misorientation-axis distributions are shown in the top right corners. See text for details.

texture on the development of the misorientation distributions, so-called “uncorrelated” (or texture-derived) misorientation-angle distributions were also calculated and are shown by solid lines in Fig. 9. In contrast to the GB misorientation distributions displaying the misorientation data between neighboring pixels in an EBSD map, the uncorrelated distributions were calculated assuming no spatial correlation between the pixels. In other words, all possible misorientations between the sampled pixels (including non-contiguous ones) were calculated.

The misorientation distributions in different regions of the SZ are broadly similar to each other (Fig. 9) as well to the misorientation distribution in Region 3 (Fig. 5c). In all cases, the GB misorientation-angle distributions are characterized by a sharp low-angle peak, a much broader irregular maximum in the angular range of $\sim 5\text{--}60^\circ$ and a wide gap in the misorientation interval of $\sim 60\text{--}93.8^\circ$. On the other hand, all the GB misorientation-axis distributions are characterized by dense clusters near the $\langle 0001 \rangle$ and $\langle 2\bar{1}\bar{1}0 \rangle$ poles, these clusters being produced mainly by the $5\text{--}30^\circ$ and $5\text{--}60^\circ$ boundaries, respectively. The area fraction of the twin boundaries is less than 1% in all cases. Of particular importance is the observation that the GB misorientation-angle distributions match reasonably well with the uncorrelated distributions in the angular range of $\sim 5\text{--}93.8^\circ$ (Fig. 9). The good correlation between the distributions means that the GB misorientation distribution may be explained in terms of the developed texture.

Formation of the partial P-fiber texture in the SZ means that the $\langle 11\bar{2}0 \rangle$ slip direction is aligned with the shear direction (Table 2) and hence grains are arbitrarily rotated around this axis with the maximal intensity in the angular interval \sim from about -10° to -20° to about $+50$ to $+60^\circ$ (Fig. 8b). Therefore, the broad irregular maximum in the angular range of $\sim 5\text{--}60^\circ$ (and the gap beyond $\sim 60^\circ$) as well as the dense cluster near the $\langle 2\bar{1}\bar{1}0 \rangle$ pole simply result from the partial P-fiber texture developed in the SZ. On the other hand, the crystallographic preference of the $5\text{--}30^\circ$ $\langle 0001 \rangle$ boundaries may also be associated with the prism slip, as discussed in Section 3.3.1. It should be added that the maximal rotation angle around $\langle 0001 \rangle$ (associated with the prism slip) is 30° due to limitations imposed by the symme-

try of the hcp crystal structure. Thus, the specific nature of the misorientation distributions in the SZ may be attributed to the stir zone texture.

3.4.4. Texture–microstructure relationship

Neither structure morphology nor texture and misorientation distribution change principally in the SZ (Figs. 6, 8 and 9) and the microstructure evolution is thus mainly reflected by the variation of the HAB spacing, texture strength and LAB fraction (Table 3). Direct comparison of the evolutions of these parameters in the SZ indicates some correlation between them: the texture strengthening from the RS to AS is accompanied by increases in the LAB fraction and HAB spacing. This may indicate that the texture formation and the development of the grain boundaries in this region are closely linked.

Generally, the texture formation means that the crystallographic orientations of many grains become close. If the texture is strong, the orientation difference between neighboring grains may become low and some of them may even converge. In this case, the misorientation across their boundaries decreases into the low-angle range, thus increasing the total LAB fraction and average HAB spacing. In other words, if the texture is sufficiently strong ($\sim 16\text{--}18$ times random, as shown in Table 3), it may exert a significant influence not only on the grain boundary misorientation (as shown in the previous section), but also on the grain size and structure morphology.

It may be thus hypothesized that the formation of the very specific grain structure (which is dominated by the LAB/HAB mixture) in Region 3 and in the SZ is mainly

Table 3

Average HAB spacing, HAB fraction and texture strength in different regions of SZ.

Microstructural region	Texture strength ^a (times random)	LAB fraction (%)	Average HAB spacing (μm)
RS	16	42	4.6
Center	19	53	8
AS	18	53	8.6

^a The texture strength corresponds to the maximal intensity observed in $\langle 0002 \rangle$ pole figures.

associated with the development of a strong texture during FSW. In other words, the grain structure evolution in these regions is thought to be mainly governed by the texture-induced grain convergence.

4. Conclusions

The present study examined the grain structure evolution during FSW of commercial purity titanium. The global straining state during the process was deduced to be close to the simple shear with the shear surface being nearly along the truncated cone having a diameter close to that of the tool shoulder in the top part of the SZ and the pin diameter in the bottom part of the SZ. The material flow was shown to arise mainly from the prism slip, giving rise to the pronounced P-fiber $\{hkil\}\langle 11\bar{2}0\rangle$ simple shear texture in the SZ. The grain structure evolution was shown to be a complex process driven mainly by the texture-induced grain convergence, but also involving the geometrical effects of strain and limited discontinuous recrystallization. The development of the deformation-induced grain boundaries in the SZ was demonstrated to be dictated by the texture evolution.

Acknowledgments

The authors are grateful to Mr. A. Honda and Dr. Y. Zhang for technical assistance. One of the authors (S. Mironov) would like to express his hearty thanks to the Japan Society for the Promotion of Science and to Tohoku University for providing a scientific fellowship. Financial support from the Japanese Ministry of Education, Science, Sports and Culture with a Grant-in-Aid from the Global COE

Program in Materials Integration International Center of Education and Research at Tohoku University is also gratefully acknowledged.

References

- [1] Thomas WM. Friction stir butt welding. International patent PCT/GB92/02203; 1991.
- [2] Mishra RS, Ma ZY. Mater Sci Eng R 2005;50:1.
- [3] Prangnell PB, Heason CP. Acta Mater 2005;53:3179.
- [4] Fonda RW, Bingert JF, Colligan KJ. Scripta Mater 2004;51:243.
- [5] Mironov S, Sato YS, Kokawa H. Acta Mater 2008;56:2602.
- [6] Reynolds AP, Hood E, Tang W. Scripta Mater 2005;52:491.
- [7] Park SHC, Sato YS, Kokawa H. Metall Mater Trans A 2003;34:987.
- [8] Lienert TJ. In: Mishra RS, Mahoney MW, editors. Friction stir welding and processing. ASM International; 2007. p. 123.
- [9] Lee W-B, Lee C-Y, Chang W-S, Yeon Y-M, Jing S-B. Mater Lett 2005;59:3315.
- [10] TSL. OIM version 3.0. On-line help. Draper, UP: TSL; 2001.
- [11] Sato YS, Kokawa H, Enmoto M, Jogan S. Metall Mater Trans A 1999;30:2429.
- [12] Hurley PJ, Humphreys FJ. Acta Mater 2003;51:1087.
- [13] Li B, Godfrey A, Meng QC, Liu Q, Hansen N. Acta Mater 2004;52:1069.
- [14] Hughes DA, Hansen N. Acta Mater 1997;45:3871.
- [15] Mironov SYu, Salishchev GA, Myshlyaev MM, Pippin R. Mater Sci Eng A 2006;418:257.
- [16] Prangnell PB, Hayes JS, Bowen JR, Apps PJ, Bate PS. Acta Mater 2004;52:3193.
- [17] Hansen N, Jensen DJ. Philos Trans R Soc Lond A 1999;357:1447.
- [18] Prangnell PB, Bowen JR, Apps PJ. Mater Sci Eng A 2007;375-377:178.
- [19] Kuhlmann-Wilsdorf D, Hansen N. Scripta Metall Mater 1991;25:1557.
- [20] Beausir B, Toth LS, Neale KW. Acta Mater 2007;55:2695.
- [21] Li S. Acta Mater 2008;56:1031.
- [22] Knipling KE, Fonda RW. Scripta Mater 2009;60:1097.